Nanoscale

REVIEW

View Article Online
View Journal | View Issue

Cite this: *Nanoscale*, 2023, **15**, 11746

Progress on the *in situ* imaging of growth dynamics of two-dimensional materials

Xiaokai Zhu, [a,b] Honggang Wang,[a,b,c] Kangkang Wang [a,b] and Liming Xie *[a,b]

Received 30th March 2023,
Accepted 20th June 2023

DOI: 10.1039/d3nr01475d

rsc.li/nanoscale

One key issue to promote the industrialization of two-dimensional (2D) materials is to grow high-quality and large-scale 2D materials. Investigations of the growth mechanism and growth dynamics are of fundamental importance for the growth of 2D material, in which *in situ* imaging is highly needed. By applying different *in situ* imaging techniques, details for growth process, including nucleation and morphology evolution, can be obtained. This review summarizes the recent progress on the *in situ* imaging of 2D material growth, in which the growth rate, kink dynamics, domain coalescence, growth across the substrate steps, single-atom catalysis, and intermediates have been revealed.

1. Introduction

The discovery of atomically thin graphene films by Novoselov *et al.* in 2004 has boosted the research on two-dimensional (2D) materials.[1] So far, many branches of 2D materials have been identified including graphene,[1] hexagonal boron nitride (h-BN), transition metal dichalcogenides (TMDs, such as MoS_2,[2] WTe_2,[3] WSe_2,[4] and ReS_2 [5]), black phosphorus (BP),[6] transition metal halides,[7] metal thio/selenophosphates,[8] transition metal carbides and nitrides (MXenes)[9,10] and so on.[11–15] Due to their atomic thickness, dangling-bond free surfaces, and unique electronic structures, 2D materials have been endowed with novel physical properties such as massless fermions,[16] Ising superconductivity,[17] quantum Hall effect,[18] *etc*. As a result, extensive effort has been made to explore the fundamental science as well as the electronic applications of 2D materials.

Toward the fundamental research and potential device applications, it is highly demanded to synthesize 2D materials with high quality and high uniformity in a large area. Besides, the growth of 2D materials with precise layer numbers, low density of defects, and desired crystal orientations is more desirable. To date, 2D materials have been grown by physical vapour deposition (PVD),[7] molecular beam epitaxy (MBE),[19] atomic layer deposition (ALD),[20] chemical vapour deposition (CVD),[21,22] metal–organic CVD (MOCVD),[23] and so on. To meet

[a]*CAS Key Laboratory of Standardization and Measurement for Nanotechnology, National Center for Nanoscience and Technology, Beijing 100190, P.R. China. E-mail: xielm@nanoctr.cn*
[b]*University of Chinese Academy of Sciences, Beijing 100049, P.R. China*
[c]*Department of Chemistry, Tsinghua University, Beijing 100084, China*

Xiaokai Zhu

Xiaokai Zhu obtained his B.Sc. in chemistry from Huazhong University of Science and Technology in 2017. Currently he is a Master student at National Center for Nanoscience and Technology. His research interest focuses on the synthesis of 2D materials as well as the understanding of their growth mechanisms.

Liming Xie

Dr Liming Xie is currently a professor at National Center for Nanoscience and Technology (NCNST, China). He received his Ph.D. degree from Peking University in 2009 and during which he went to MIT as a visiting student in 2007–2008. He did his postdoctoral research at Stanford University in 2009–2012 and joined NCNST as a professor in 2012. His research interest is on synthesis, Raman spectroscopy and devices of 2D materials.

the requirements, a thorough understanding of the growth mechanisms and the precise measurement of the growth dynamic parameters are needed. So far, *ex situ* experiments and simulations have been implemented to gain information about the growth mechanisms and growth dynamics.[24–29] However, *ex situ* experiments require to interrupt the growth process, which is time-consuming and also cannot exclude the growth or etching during the cooling down process. Alternatively, *in situ* imaging of the growth is more preferred to capture the chemical and physical process in real-time. The generally used *in situ* techniques are presented in Fig. 1, including transmission electron microscopy (TEM), scanning electron microscopy (SEM), scanning tunnelling microscopy (STM), optical microscopy, X-ray photoelectron spectroscopy (XPS), X-ray diffraction (XRD), X-ray reflectivity (XRR), spectroscopic ellipsometry, differential reflectance spectroscopy (DRS) and Raman spectroscopy. Growth dynamics covering nucleation event, domain coalescence, and so on can be directly imaged. Further information, such as kink dynamics, can also be evaluated by model analysis and data fitting. All the growth dynamics information is critical for finely controlling the growth of 2D materials.

However, there are difficulties in visualizing and imaging of the growth process. For example, the high temperature environment prevents a close imaging of the growth. Additionally, electron microscopic techniques require a vacuum condition. So, in most cases, a mini high-temperature stage/reactor is customized and put inside or under the characterization tools. In very few cases, the characterizations can also be directly used with the growth furnace/chamber, such as low energy electron microscopy (LEEM), DRS, and XPS. Using these *in situ* techniques, the nucleation events, evolution of crystal morphology/structures/chemical compositions during the material growth can be revealed.

In this review, we have summarized the recent progress on the *in situ* investigations of the growth dynamics of 2D materials. To begin with, the used techniques are briefly introduced. And then, the growth dynamics of 2D materials revealed by these *in situ* characterizations are discussed in detail, including growth rate, kink dynamics, domain coalescence, growth crossing the substrate steps, single-atom catalysis, and intermediates. At last, further research and challenges in the *in situ* imaging are discussed.

2. Characterization techniques used for *in situ* investigation

2.1. Imaging techniques

TEM offers atomic-scale insight into the nucleation, kink advancement, defect formation, atom diffusion, evolution of grain boundaries, and so on. To achieve *in situ* TEM imaging, a specially designed specimen holder is required.[30] In most cases, *in situ* heating for TEM are realized by placing a heating element at the end of the specimen holder and using precise Joule heating and temperature dissipation to obtain precise and stable specimen temperatures.[31] In 2005, Zhang *et al.* designed a micro electro-mechanical system (MEMS) device as a heater and a specimen carrier to observe the melt of bismuth nanoparticles.[32] A thin film fabricated on the MEMS heater is used for heating by applying electric current.[33] This thin film is usually made of metal, ceramic, or doped polysilicon. Very recently in 2023, Zhao *et al.* designed a sample holder with a 2D graphene based microheater, which can heat up the stage rapidly with less energy, and low thermal expansion at higher temperatures.[34] Moreover, by integrating a microfabricated gas cell together with the MEMS heater, *in situ* characterizations in reactive gaseous and elevated temperature

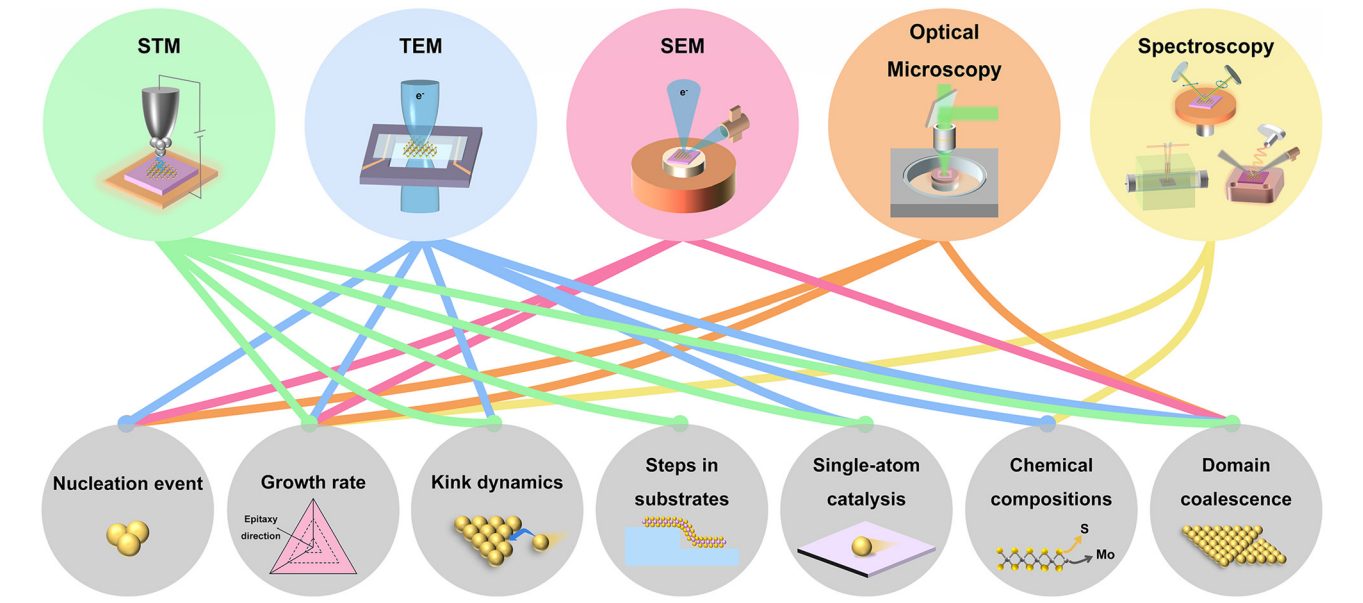

Fig. 1 Schematic illustration of the used *in situ* techniques for 2D materials growth and the related research on the growth dynamics.

environment are both allowed. Nowadays, *in situ* studies are majorly conducted on such multi-functional reactors.[33,35,36]

SEM utilizes a focused electron beam to scan over samples. The incident electrons generate secondary electrons (SE) and backscattered electrons (BSE) which carry rich information about the surface morphology and chemistry compositions of the sample. Similar to *in situ* TEM imaging, a specimen stage is designed for *in situ* SEM imaging. So far, numerous strategies have been implemented to heat the *in situ* stages, such as laser heating,[37] current heating,[38] and metallic coil heating.[39] However, at the growth temperature, the thermal electrons emission from the heating element may induce interference to the *in situ* imaging.[40] To reduce the thermal electrons, methods such as changing the composition for the specimen holder,[41] encapsulation of the heating wires, and adjusting an electron filter systems are used.[42] *In situ* SEM has been applied to investigate the growth behaviours of graphene on different polycrystalline metal substrates. By collecting secondary electron signal, graphene with different layers could be discriminated from the different contrasts.[43–47]

To implement STM imaging, an atomically sharp tip is taken close to a conductive surface. Collecting the feedback of tunnelling current, atomic-resolution surface structure can be obtained. In real time characterization of growth process, thermal drift of the tip becomes severe. Hoogeman *et al.* designed a thermal-drift compensated piezoelectric scanner with a customized sample holder and then the thermal drift could be drastically reduced.[48] Additionally, the scan speed has also been improved by increasing the mechanical resonances frequencies and the bandwidth of the feedback electronic components.[49–51] In recent years, the behaviour of the atoms catalysis, the structure of crystal or edges, and different growth modes have been unveiled precisely by *in situ* STM imaging.[51–56]

With a sub-μm resolution and a large imaging field, optical microscopy is applied to recognize the nucleation sites, identify the layer number, visualize the growth process and domain coalescence, and track the morphology evolution, which can provide indispensable information for the growth dynamics. Compared with other techniques, optical microscopy can be operated under non-vacuum conditions and in a non-destructive way.[57] Usually, a mini CVD chamber with a transparent optical window is needed for *in situ* optical imaging. In 2013, Puretzky *et al.* achieved real-time optical imaging of the growth of graphene on Ni substrate.[58] And then in 2015, a radiation-mode optical microscopy was developed for imaging the growth of graphene on Cu substrate.[59] Rasouli *et al.* designed a small-sized CVD chamber which could be put under a microscope lens to realize real-time observation. With this system, vapour–solid–solid growth and vapour–liquid–solid growth of 2D TMDs were observed.[60]

2.2. Spectroscopic techniques

Raman spectroscopy is a powerful and convenient tool to characterize material structures, chemical compositions, and so on. Usually, *in situ* Raman spectroscopy is a complementary tool with *in situ* optical microscopy. Thus, to conduct *in situ* characterizations, design of the reaction chamber is the same with *in situ* optical microscopy.[58,61,62] However, at high temperatures, Raman signal becomes weaker and the thermal-emission background gets stronger. Usually, a short wavelength excitation is used to reduce the background interference. With Raman spectroscopy, layer number, compositions of intermediates, and final materials can be revealed.[63,64]

X-ray characterization can identify crystal structures (by XRD), analyse surface elemental information (by XPS), and measure the electron density profile of materials and thickness of the film (by XRR). A small reactor is put in the equipment to conduct *in situ* characterizations. Recently, *in situ* XPS and XRD have been used to follow dynamic process such as the growth of MoS_2,[65] graphene,[62,66] and 2D boroxine framework.[67] As for *in situ* XRR, Jankowski *et al.* used this method to study the growth of graphene on molten Cu foil[62,68] In 2020, Saedi *et al.* designed a CVD reactor which was integrated with an *in situ* optical microscopy, Raman, XRD, and XRR for real time investigations.[66]

Spectroscopic ellipsometry and DRS are remote and non-destructive analysis techniques. Spectroscopic ellipsometry can measure the compositions, film thickness, and growth rate and DRS can measure the compositions, growth rate, and electron state. Both spectroscopic techniques can be carried out under atmospheric pressure. So, a small CVD reactor is usually needed for *in situ* spectroscopic ellipsometry and DRS characterizations. Losurdo *et al.* applied *in situ* spectroscopic ellipsometry to clarify the effects of cleaning and annealing of metal substrate and carbon coverage at the surface on the growth behaviours. By controlling this process, precise graphene thickness was achieved.[69] *In situ* DRS can be applied in a real CVD reaction. Recently, Wang *et al.* built an *in situ* DRS system to monitor the growth process in a CVD furnace. A quartz window was designed on the top of the furnace which allowed the incident light beam to enter into the furnace.[70]

3. *In situ* investigation of 2D material growth

3.1. Imaging of the growth rate

The most straightforward information obtained *via in situ* techniques is the growth rate and its dependence on the temperature, gas flow rate, precursor, substrate, and so on.[47,59–61,71–78] In 2015, the growth and etching of graphene on Cu substrate were observed by the radiation-mode optical microscopy (Rad-OM). Bright patches of graphene grains were clearly recognized (Fig. 2a). Typical time evolution of representative grain area at 985 °C was plotted in Fig. 2c in blue. Accurate graphene growth rates with different gas flow rates and different growth temperatures were extracted. For example, by increasing CH_4 flow rates from 6 to 10 sccm, growth rates were first accelerated and then saturated. From the temperature dependence of growth rates, the activation energy was obtained, which suggested that the incorporation

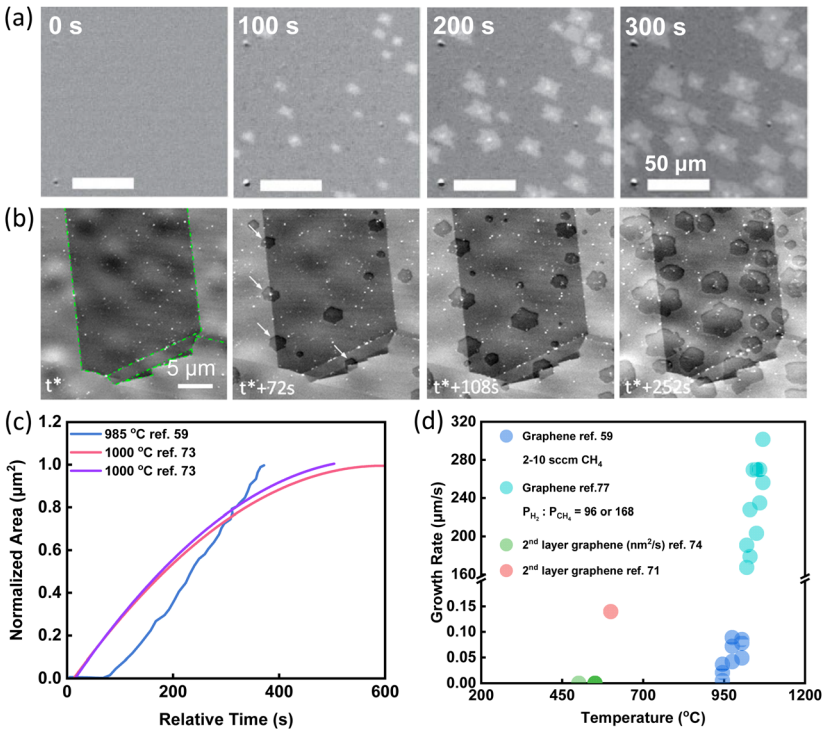

Fig. 2 Schematic illustration of *in situ* imaging the growth rate of graphene. (a) Time-series SEM images of graphene growth with the CH_4 flow rate of 5 sccm at 985 °C. Reproduced from ref. 59 with permission from Springer Nature, copyright 2015. (b) Time-series SEM images of graphene growth with C_2H_4 flow rate of 0.1 sccm at 1000 °C. White arrows highlight nucleation events at grain boundaries. *t** corresponds to the induction period from C_2H_4 dosing until the first nucleation event was detected. Reproduced from ref. 73 with permission from American Chemical Society, copyright 2015. (c) A summary of the growth pattern of graphene showing the increase of the graphene areas with time from different research works. (d) A summary of growth rates of graphene obtained under various conditions from different research work.

of precursor to graphene was the rate-determining reaction in the growth.[59]

In situ SEM has also been used to evaluate the growth rates of graphene. The entire CVD process was observed *via in situ* SEM imaging. The growth was divided into three stages. Formation of new flakes was captured by *in situ* SEM (Fig. 2b) and growth rates were quantified based on *in situ* SEM data (Fig. 2c). During the first attachment-limited growth stage, the radial growth of graphene sheets was roughly constant. With the consumption of locally supersaturated precursor, a depletion zone appeared at the growth front leading to the second surface-diffusion-limited growth stage. When the growth fronts of neighbouring graphene approached to an approximate 3 μm interval, growth evolved to the third stage and the growth rates declined rapidly.[73]

In situ spectroscopy was also used to get a rough growth rate for graphene. Tsakonas *et al.* applied *in situ* DRS to plot the values of differential reflectance $\Delta R/R_0$ as a function of time. From the graph, the growth rates were finally quantified, indicated by cyan circles in Fig. 2d.[77]

Except for graphene, the growth dynamics of 2D van der Waals CdI_2 and PbI_2 on WS_2, MoS_2 and WSe_2 was investigated. A custom-made system was used for *in situ* observation and Raman characterization of heterostructures growth dynamics. Sapphire with pre-grown WS_2, MoS_2 and WSe_2 was used as substrates for the growth of CdI_2 and PbI_2. Two growth behaviours were observed depending on the temperature of substrate. At 285 °C, CdI_2 nucleated on the WS_2 flake. After 30 s growth, the nucleus grew and evolved into a hexagonal shaped crystal. When the edge of CdI_2 reached the edge of WS_2, the growth stopped (Fig. 3a). The time evolution of the domains showed a growth rate of 0.41 μm s^{-1}. By decreasing the temperature to 260 °C, CdI_2 grew with a suborbicular shape with no clearly defined facets (Fig. 3b). The size of CdI_2 domains increased with time in a sublinear fashion and the growth rate slowed down as domain size increased. Based on the *in situ* images, their different growth patterns and rates have been concluded in Fig. 3c. The different growth behaviours at different temperatures were originated from the temperature-dependent surface diffusion and edge adsorption effects.[76]

Very recently, our group applied a high-temperature optical microscope equipped into the CVD furnace[79] to record the *in situ* growth process and developed a new liquid phase edge epitaxy method (LPEE) in Fig. 3d. In this new growth method, MoS_2 contacted the liquid only at the edges and the growth was confined only along the MoS_2 edges, resulting in precise-monolayer epitaxy of TMDs. Moreover, with the evolution of the flakes, the size of the liquid droplet decreased simultaneously, thus, indicating that the evaporation of the solvent

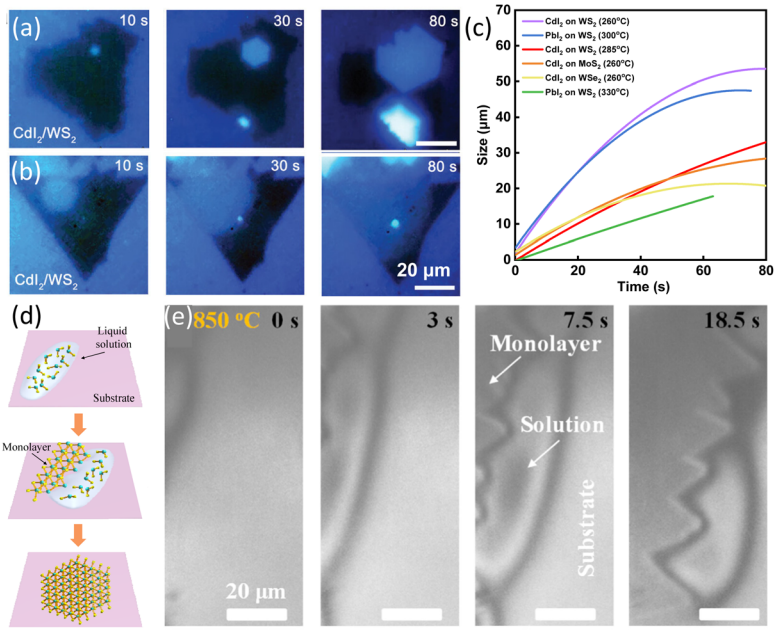

Fig. 3 Schematic illustration of *in situ* imaging the growth rate of MI_2 (M = Cd, Pb) and MoS_2. (a) *In situ* real-time images of the growth process of CdI_2/WS_2 heterostructure at a growth temperature of 285 °C. (b) *In situ* real-time images of the growth process of CdI_2/WS_2 heterostructure at a growth temperature of 260 °C. (c) Plotting of the size of MI_2 (M = Cd, Pb) with time at different temperatures. Reproduced from ref. 76 with permission from Wiley, copyright 2021. (d) Illustration of the LPEE process of TMDs. (e) *In situ* imaging of LPEE of MoS_2 monolayers from the CsCl solution at 850 °C. Reproduced from ref. 78 with permission from American Chemical Society, copyright 2023.

was the driving force. The epitaxy rate was measured to be 1–2 μm s^{-1}.[78]

3.2. Imaging of the kink dynamics

Based on the classic terrace-step-kink (TSK) model, the growth process includes adatom diffusion, nucleation and dynamics of the stable nucleus, atom attachment to create kinks, and kinks propagations along the edge. In particular, kinks are the most important and active sites for adding or removing atoms.[24] Under a low supersaturation condition, kink generation can be the rate-limiting process.

To elucidate how kinks form and how kinks advance, *in situ* STM was used to record the growth of h-BN (Fig. 4b and c). At the beginning, the shape of h-BN was a hexagon with three short edges and three long edges corresponding to a high energy and a low energy edge. The edges with higher energy disappeared quickly, forming a truncated triangular (Fig. 4b). *In situ* STM revealed that different kink creation rate contributed to the disappearance of the edges. New nanomesh units formed at kink sites and then moved along the edges. Kinks advanced along both edges at an equal speed.[80]

In 2013, Dong *et al.* imaged the kink dynamics in the growth of graphene on Rh(111). The growth started from creation of kinks and then the kinks advanced along the edge in units of the moiré pattern which consisted of 288 carbon atoms. And this observation was quite similar with the previous work on the growth of h-BN.

Kink advancement and kink creation at concave conners were also investigated. Kink creation rate at the concave conner depended on the corner angle (Fig. 4h and i). The kinks were created faster at the 60° concave corner and slower at the concave corners with angles larger than 120°.[52]

Wang *et al.* studied the kink-accelerated growth during the domain coalescence of graphene *via in situ* SEM characterizations. When two zigzag edges domains met, a concave corner with an angle of 120° formed. Then, fast attachment of growth species at the concave corner led to the formation of a new growth front (Fig. 5c–f). The edge of the new front was tilted 19.1° with respect to the initial zigzag edge, indicated in Fig. 5g. This edge had the highest possible kink density which was coincided with the theoretical simulations by Ma *et al.*[24] Thus, this edge became the fastest growing edge during attachment-limited growth. Simulations of growth process at this concave angle presented in Fig. 5g was in accordance with the observation.[81]

These *in situ* investigations have revealed the important role for the kinks. During the growth, the creation of kinks determines the growth rate. Besides, when two domains coalesce, the shape of the final flake is affected by kinks. More *in situ* studies are needed to quantify the exact relationship between the kink concentrations and growth rates.

3.3. Imaging of the domain coalescence

One of the most possible strategies to obtain wafer scale single crystals of 2D materials is the seamless coalescence of small single-crystalline domains.[82–85] After coalescence, there may be grain boundaries which play an important role in the device performance.[86] The domain coalescence process has

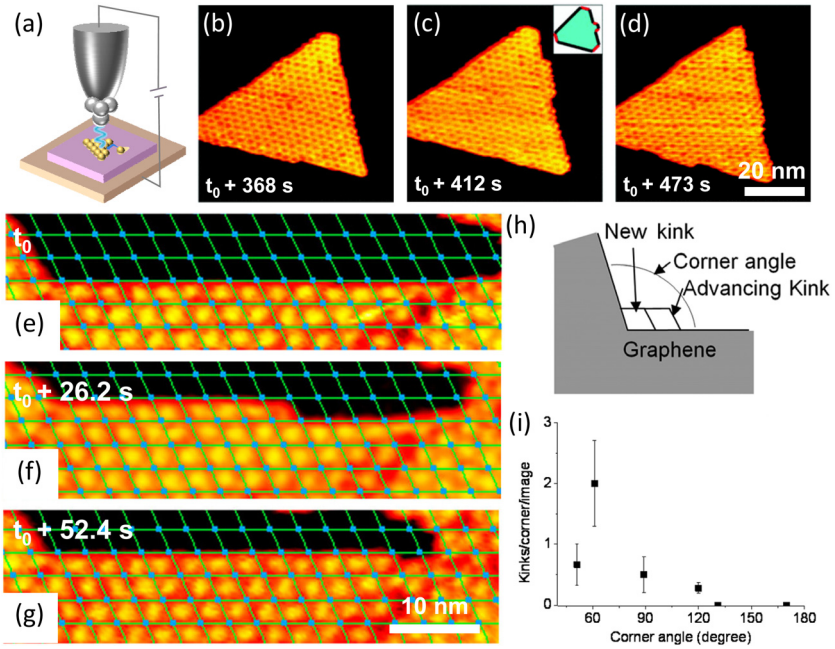

Fig. 4 Schematic illustration of *in situ* imaging of kink dynamics at the edge during the growth of h-BN and graphene. (a) Diagram of an *in situ* scanning tunnelling microscope. (b–d) Sequential STM images of h-BN growth on Rh(111) with borazine precursor at 978 K. Reproduced from ref. 80 with permission from the American Physical Society, copyright 2010. (e–g) Sequential STM images for graphene growth at 975 K on Rh(111) with an ethylene pressure of 5.7×10^{-9} mbar. (h) Sketch of kink creation at a concave graphene corner and subsequent kink advancement. (i) Measured average number of kink creation events per STM image as a function of the angle of the concave graphene corner. Reproduced from ref. 52 with permission from American Chemical Society, copyright 2013.

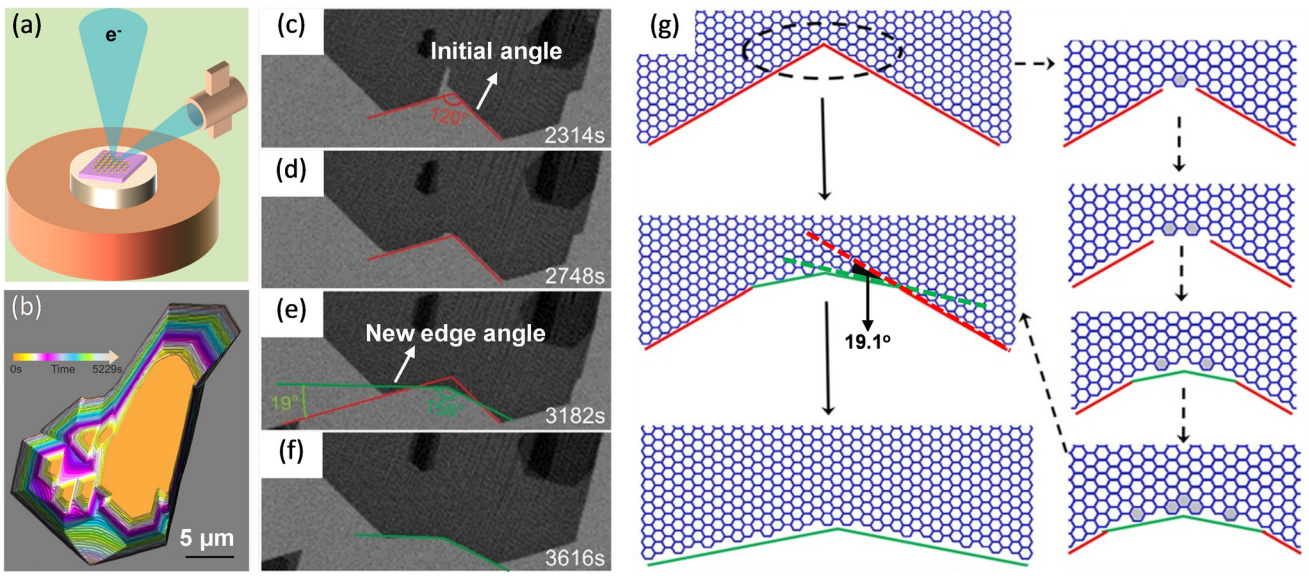

Fig. 5 Schematic illustration of *in situ* imaging of kink dynamics at the concave corner during the growth of graphene. (a) Diagram of an *in situ* scanning electron microscope. (b) Shape evolution of the graphene domains during coalescence. (c–f) Sequential images showing the appearance of new edges at the concave corner during the coalescence. The new growth fronts which were tilted with a 19.1° dip angle. (g) Atomistic model of the growth process of a concave corner with an angle of 120° and zigzag edges in the case of well-aligned graphene domains. Reproduced from ref. 81 with permission from American Chemical Society, copyright 2020.

been observed by *in situ* STM,[80,87] TEM,[88,89] SEM,[81] and optical microscopy.[62] Liu *et al.* monitored the coalescence of graphene on Cu by *in situ* TEM. As the two grain boundaries with different crystallographic orientations moved closer, their grain edges contacted quickly but remained their original orientations. Hence, a clear grain boundary was formed.

However, after 0.5 s, two grains reoriented and completely merged together. The grain boundary disappeared, resulting in a single grain with the same crystallographic orientation. This fast merge-reorientation phenomenon is explained by the first-order phase transition of the local atoms. *In situ* imaging also showed that the defects for the as-grown graphene could be repaired during growth.[89]

Jankowski *et al.* used *in situ* Rad-OM to monitor the growth behaviour of graphene on liquid copper at 1370 K. The whole growth process was demonstrated in Fig. 6a–d. During the growth, the flakes grew larger and flew close to each other, indicating the presence of an attractive long-range interaction between the domains. However, when the domains moved closer to each other (20–40 μm), there appeared a short-range repulsive interaction between them which kept the grains evenly distributed on the liquid copper. As the growth further proceeded, continuous and domain-boundary-free graphene film was formed eventually.[62]

These findings have elucidated the effect of substrates during the coalescence of graphene. Seamless graphene films were obtained both on Cu films and on liquid copper *via* different mechanisms. For TMDs, the investigation in the domain coalescence is far more limited.

Sang *et al.* observed the oriented attachment of nanograins during the growth of 2D MoS_2 *via* thermolysis of $(NH_4)_2MoS_4$. The nanograins were initially formed at 600 °C. As shown in Fig. 6e–h, the middle grain slowly moved toward the left grain. After the middle grain attaching to the left grain, the middle grain reoriented to align with the left grain to reduce the total energy. In contrast, the right grain moved toward the middle grain but kept its orientation after attaching to the middle grain due to its larger size and hence a higher energy barrier for reorientation.[88]

3.4. Imaging of crossing over the substrate steps

Recently, the step-edge-guided method has shed light on the large-scale growth of single crystal 2D materials. Atomic steps on the vicinal surface of the substrate guide a unidirectional domain growth. Domains with the same orientations finally merge into a single crystalline thin film. Consequently, the understanding of how substrates and steps affect the growth process is needed.

In 2011, Günther *et al.* observed a downhill growth mode for graphene using *in situ* STM. The collected data demonstrated that graphene preferentially grew across the descending steps with a carpet-mode.[90] However, the graphene grown on the lower terrace was from the pointlike seeds at the step edge. These seeds led to different orientations of the graphene. At a low pressure and a high temperature, the Ru terraces moved with the front of graphene edges, and hence the graphene did not grow downhill across the atomic steps. Instead, this yielded large-size terraces and perfectly crystalline graphene films.[91]

Uphill and downhill growth modes were both observed by *in situ* STM imaging under different growth conditions for the growth of h-BN on Pd(111) surface (Fig. 7a and b). At a low temperature, due to a lower effective activation barrier at step sites, the nucleation and growth of h-BN occurred majorly at the ascending steps in spite of large terrace areas. The growth obeyed an uphill growth mode. Differently, at a high temperature and a low pressure, the deposition rate at terrace sites increased exceeding the deposition rate at step edges. Hence, the growth occurred on terraces. Since the growth at the descending Pd steps was kinetically suppressed, h-BN islands formed on terraces eventually followed a downhill growth mode.[56]

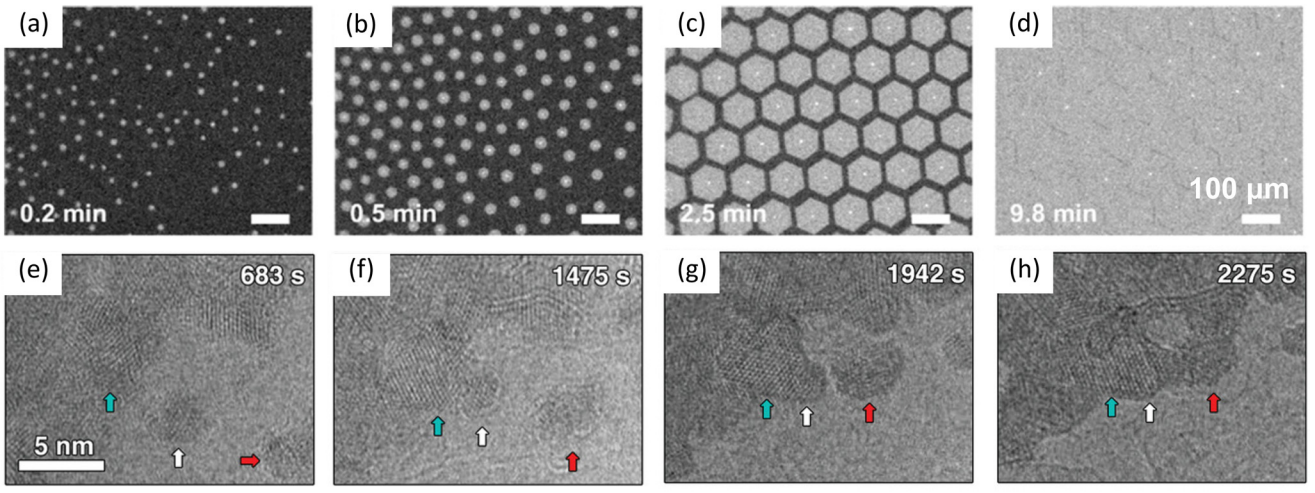

Fig. 6 Schematic illustration of *in situ* imaging of domain coalescence processes during graphene growth and MoS_2 growth. (a–d) *In situ* optical imaging of graphene growth on liquid copper. Reproduced from ref. 62 with permission from American Chemical Society, copyright 2021. (e–h) TEM images showing coalescence of MoS_2 grains. Grains indicated by white and red arrows move toward the grain indicated by cyan arrow. Reproduced from ref. 88 with permission from Wiley, copyright 2019.

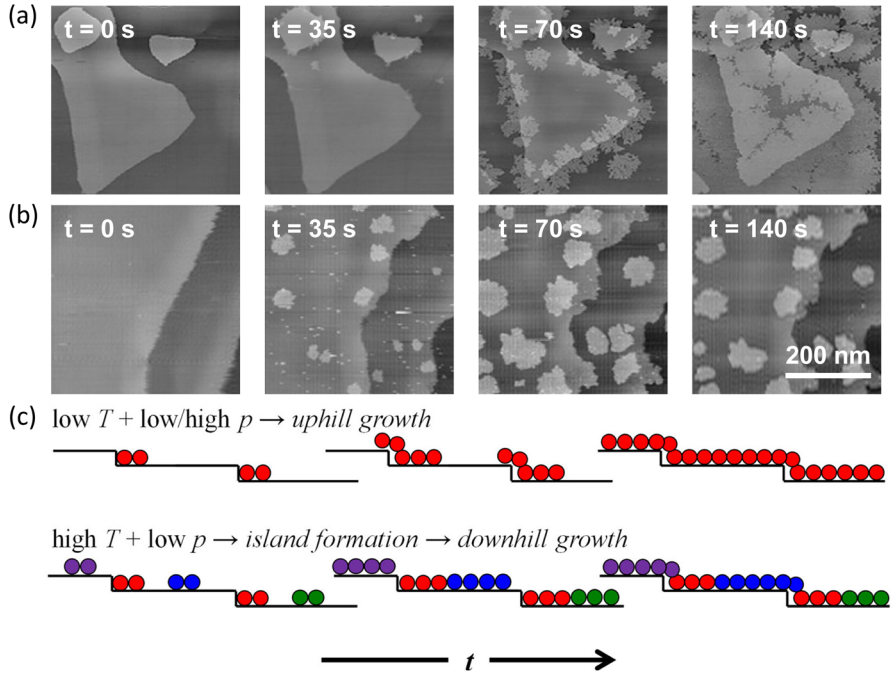

Fig. 7 Schematic illustration of *in situ* imaging of the h-BN growth across the substrate steps. (a and b) Representative *in situ* STM images acquire during the CVD growth of h-BN on Pd(111) at (a) temperature T = 573 K, borazine pressure p = 10^{-6} mbar and (b) T = 673 K, p = 10^{-7} mbar. Deposition times t indicated in the image panels are with respect to an arbitrary time during annealing the sample at the set T in UHV, at which borazine is introduced into the STM system. (c) Schematic of the h-BN growth modes at different deposition conditions. Different colours correspond to different rotational domains of h-BN. Reproduced from ref. 56 with permission from American Chemical Society, copyright 2020.

Overall, these studies have suggested that the growth across steps relied on the substrates, the growth temperature, precursor pressure, and so on.

3.5. Imaging of single-atom catalysis

Single-atom catalysts have compelling potentials because each atom is accessible for the catalytic reaction with 100% atomic efficiency. Many studies have evidenced that single atoms will participate in the growth of graphene on metal substrates.[92] The catalysis involves the connection of single atoms to the edge of 2D materials. And then, the growth (*i.e.*, atom attachment) is catalysed at the catalysis site.

In 2014, Liu *et al.* applied atomic resolution aberration-corrected STEM to investigate the graphene growth and domain boundary formation under electron-beam irradiation. During the second layer graphene growth, single Si atoms as catalyst were observed unexpectedly. A series of annular dark-field (ADF) images were captured by *in situ* TEM at 500 °C (Fig. 8a–d). On the left side of the dashed magenta line was the initial second layer of the graphene. A tip-growth mechanism could be observed, in which graphene grew next to Si atoms and Si atoms were pushed to the edge front.[74]

Single Si atoms were also observed to catalyse the dissociation of carbon atoms from graphene in an aberration-corrected HRTEM.[93] Several more research has been published to further reveal the mechanisms of single Fe,[94] Cr,[95] and Sn[96] atom catalysis on the edge of graphene using *in situ* TEM imaging.

In 2018, Patera *et al.* directly visualized the growth of graphene on Ni(111) and uncovered how single Ni atoms involved in growth process at kink sites of graphene. At first glance of *in situ* STM images shown in Fig. 8f and g, carbon atoms started to incorporate at the kink sites and then propagated along the edge at both the z edge and the k edge. The presence of bright objects at the kink sites, which were Ni atoms, was also recorded in the images. As the Ni adatoms reached the kinks, a carbon dimer was formed nearby (Fig. 8f and g). This observation indicated that the addition of carbon atoms at kink sites was catalysed by single Ni atoms. Combining with DFT simulations, such a high catalysis activity was ascribed to a 35% decline of the rate-limiting energy barrier of the growth process with the Ni atoms.[54]

3.6. Imaging of the intermediates

Characterizations of the intermediate species during the growth is important to understand the growth pathway.

Weatherup *et al.* uncovered how C_2H_2 was catalysed to form graphene on catalysts substrate based on *in situ* X-ray characterizations. Four intermediate steps were observed. Shortly after the introduction of C_2H_2 precursor, carbon decomposed from C_2H_2 bound to the high reactivity Ni surface sites (C_A). And then, this surface carbon diffused into the Ni subsurface forming a Ni–C solid solution (C_{Dis}). Later, graphene (C_{Gr}) and defects (C_B) emerged at the same time. Thus, a reduction of C_B peak meant a reduction of defects, amorphous carbon, and domain boundary density.[97,98]

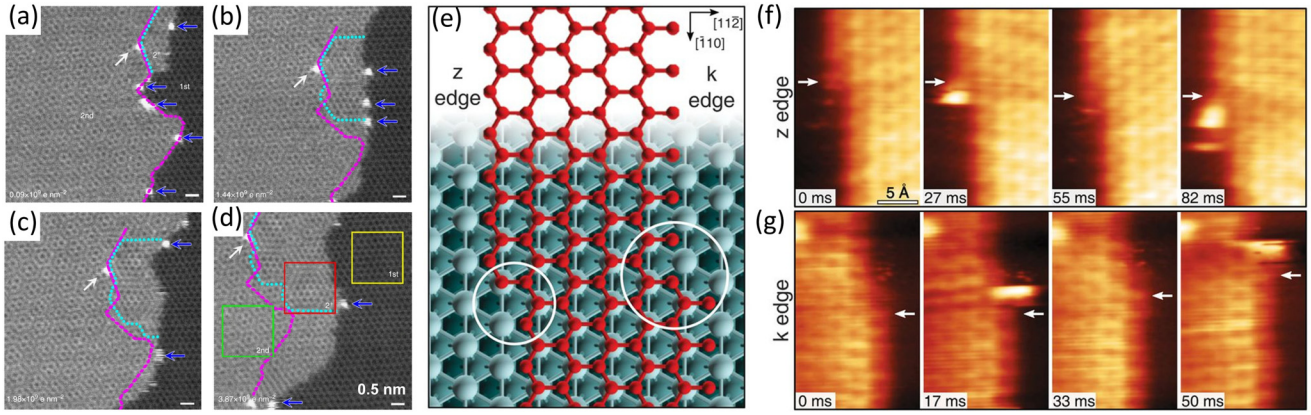

Fig. 8 Schematic illustration of *in situ* imaging of the single-atom catalysis during graphene growth. (a–d) Sequential ADF images showing graphene from the step-edge of the bilayer graphene. The initial 2nd-layer step-edge is indicated by dashed magenta line, while the rotated 2^{+}-layer highlighted by cyan dot line shows different moiré patterns and increases over time. Reproduced from ref. 74 with permission from Springer Nature, copyright 2014. (e–g) Sequential STM images during graphene growth along z and k edges. (e) Zigzag (z) and Klein (k) edges of a top-fcc epitaxial graphene layer on Ni(111). At both edges, the kink structures are highlighted by circles. (f) High-speed STM sequence acquired at 710 K in quasi-constant height mode at the z edge. White arrows indicate the position of C atoms in fcc-hollow sites near the kink. (g) Same as in (f) but for the k edge. Reproduced from ref. 54 with permission from American Association for the Advancement of Science, copyright 2018.

Combining *in situ* spectroscopy with *in situ* microscopy, the growth mechanism can be further revealed. In 2020, Xue *et al.* developed a versatile *in situ* system to investigate the sulfurization of MoO_3. The system was equipped with an *in situ* optical microscope and a confocal Raman spectrometer. At 550 °C, the Raman peaks E_{2g} and A_{1g} of MoS_2 were observed (Fig. 9a).

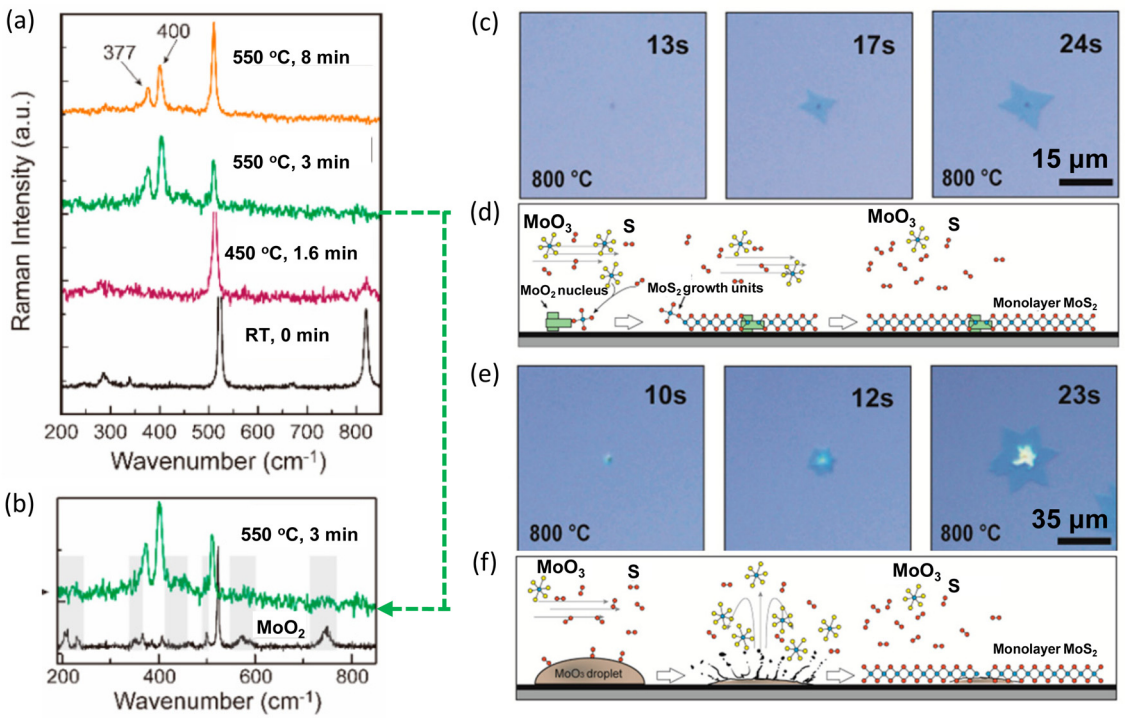

Fig. 9 Schematic illustration of *in situ* imaging of the intermediates during MoS_2 growth. (a) Raman spectra of MoO_3 with S vapours at different temperatures. (b) Raman spectrum of MoO_3 2D flakes sulfurized at 550 °C for 3 min and Raman spectrum of MoO_2 at room temperature. (c) Growth mode of MoS_2 monolayer growth around a nucleation site. (d) Schematic for MoS_2 monolayer grown around a MoS_2 nucleation site, in which the growth is fed by the vapour-state Mo sources. (e) Growth mode of MoS_2 monolayer growth from MoO_3 droplets. (f) Schematic for MoS_2 monolayer from a MoO_3 droplet, in which the growth is fed by the liquid droplet. Reproduced from ref. 61 with permission from American Chemical Society, copyright 2020.

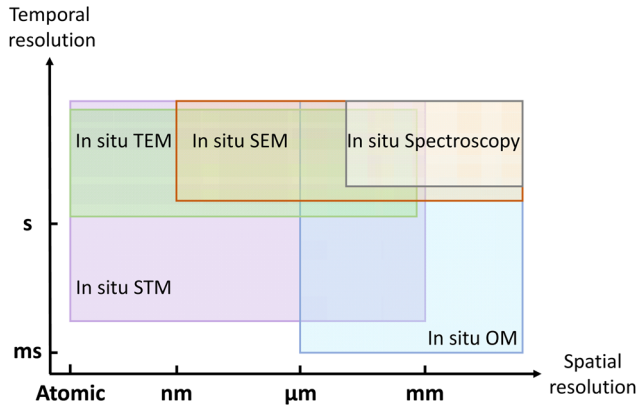

Fig. 10 Schematic illustration of the spatial resolution and temporal resolution for *in situ* techniques.

Besides, peaks belonging to the intermediates of MoO_2 or $MoOS_2$ were also detected at initial stage (Fig. 9b). Additionally, *in situ* optical imaging revealed two growth modes. One mode was MoS_2 monolayer grown around a solid nucleation site (Fig. 9c and d) and another mode was MoS_2 grown from a liquid droplet (Fig. 9e and f). The first mode grew much faster and larger because of high density of intermediate MoO_{3-x} vapours near the substrate surface, providing sufficient Mo for growth.[61]

4. Conclusions

In this review, we have introduced *in situ* techniques used for visualizing the growth of 2D materials, including imaging techniques (such as TEM, STM, SEM, and optical microscopy) and spectroscopic techniques (such as DRS, spectroscopic ellipsometry, XRD, XRR, XPS and Raman). To realize precise heating and clearly imaging simultaneously inside or under *in situ* techniques, the sample holder or heating stage should be specially designed. As shown in Fig. 10, these *in situ* techniques can track the growth process at different spatial resolutions and different temporal resolutions.

To evaluate how fast the 2D materials grow and how the morphology evolves, *in situ* optical microscope and *in situ* SEM can be the most suitable choices. *In situ* TEM can be applied to investigate the nucleation stage due to its atomic resolution. With the sensitivity to the surface, *in situ* STM can be used to visualize how 2D materials grow on the vicinal surface. *In situ* spectroscopy provides complementary information about the chemical compositions, surface information, and crystal structures. Utilizing these *in situ* techniques, the dynamic process of nucleation, edge epitaxy, single-atom catalysis, and substrate effect can be thoroughly visualized.

In spite of so many advancements, challenge remains. Firstly, compared to abundant works on *in situ* investigations in graphene and h-BN, less effort has been made in the investigations on the growth of other 2D materials, such as TMDs. The *in situ* TEM and STM studies on the growth of TMDs mentioned are based on the thermal decomposition of molybdates which is quite different from the widely used CVD reactions. The difficulties are that the growth of TMDs involves several precursors and requires more complex heating stages for *in situ* imaging.

Secondly, most of the *in situ* characterizations are not conducted in real CVD furnaces. As for *in situ* STM, *in situ* TEM, and *in situ* SEM characterizations, the equipment is generally modified with special specimen holder inside the chamber to allow the high temperature growth of 2D materials. Besides, specially designed micro-furnace or miniaturized reactor are used for *in situ* optical microscopy. In the miniaturized reaction systems, the reaction regimes and the kinetics can be quite different. Thus, characterizing the growth process in a real CVD furnace is still needed for unveiling the growth kinetics.

In the future, more effort is needed. Firstly, more advanced equipment/techniques are needed, such as STM, TEM, and, SEM with higher temporal resolution and better stability at high temperatures. Thus, key details such as nucleation behaviours, kink formation, and diffusion of the atoms can be captured to unravel the growth mechanisms. As for optical microscopy, the advent of high temperature optical microscope made it possible to monitor the CVD process in furnace.[78,79] Secondly, with the development of *in situ* techniques, more *in situ* investigations are needed to quantify the growth parameters such as nucleation rate, growth rate, diffusion rate, kink density, energy barriers, and so on.

Conflicts of interest

The authors declare that they have no known competing financial interests or personal relationships that could have appeared to influence the work reported in this paper.

Acknowledgements

The authors gratefully acknowledge the support from the Strategic Priority Research Program of CAS (XDB36000000), National Key R&D Program of China (2020YFB2205901) and the NSFC (22105049).

References

1 K. S. Novoselov, A. K. Geim, S. V. Morozov, D. Jiang, Y. Zhang, S. V. Dubonos, I. V. Grigorieva and A. A. Firsov, *Science*, 2004, **306**, 666–669.
2 K. F. Mak, C. Lee, J. Hone, J. Shan and T. F. Heinz, *Phys. Rev. Lett.*, 2010, **105**, 136805.
3 M. N. Ali, J. Xiong, S. Flynn, J. Tao, Q. D. Gibson, L. M. Schoop, T. Liang, N. Haldolaarachchige, M. Hirschberger, N. P. Ong and R. J. Cava, *Nature*, 2014, **514**, 205–208.

4 H. Fang, S. Chuang, T. C. Chang, K. Takei, T. Takahashi and A. Javey, *Nano Lett.*, 2012, **12**, 3788–3792.
5 S. Tongay, H. Sahin, C. Ko, A. Luce, W. Fan, K. Liu, J. Zhou, Y.-S. Huang, C.-H. Ho, J. Yan, D. F. Ogletree, S. Aloni, J. Ji, S. Li, J. Li, F. M. Peeters and J. Wu, *Nat. Commun.*, 2014, **5**, 3252.
6 H. Liu, A. T. Neal, Z. Zhu, Z. Luo, X. Xu, D. Tománek and P. D. Ye, *ACS Nano*, 2014, **8**, 4033–4041.
7 H. Liu, X. Wang, J. Wu, Y. Chen, J. Wan, R. Wen, J. Yang, Y. Liu, Z. Song and L. Xie, *ACS Nano*, 2020, **14**, 10544–10551.
8 K. Du, X. Wang, Y. Liu, P. Hu, M. I. B. Utama, C. K. Gan, Q. Xiong and C. Kloc, *ACS Nano*, 2016, **10**, 1738–1743.
9 M. Naguib, V. N. Mochalin, M. W. Barsoum and Y. Gogotsi, *Adv. Mater.*, 2014, **26**, 992–1005.
10 F. Shahzad, M. Alhabeb, C. B. Hatter, B. Anasori, S. Man Hong, C. M. Koo and Y. Gogotsi, *Science*, 2016, **353**, 1137–1140.
11 H. Tsai, W. Nie, J. C. Blancon, C. C. Stoumpos, R. Asadpour, B. Harutyunyan, A. J. Neukirch, R. Verduzco, J. J. Crochet, S. Tretiak, L. Pedesseau, J. Even, M. A. Alam, G. Gupta, J. Lou, P. M. Ajayan, M. J. Bedzyk and M. G. Kanatzidis, *Nature*, 2016, **536**, 312–316.
12 R. Ma and T. Sasaki, *Acc. Chem. Res.*, 2015, **48**, 136–143.
13 M. J. Kory, M. Worle, T. Weber, P. Payamyar, S. W. van de Poll, J. Dshemuchadse, N. Trapp and A. D. Schluter, *Nat. Chem.*, 2014, **6**, 779–784.
14 P. Vogt, P. De Padova, C. Quaresima, J. Avila, E. Frantzeskakis, M. C. Asensio, A. Resta, B. Ealet and G. Le Lay, *Phys. Rev. Lett.*, 2012, **108**, 155501.
15 J. W. Colson, A. R. Woll, A. Mukherjee, M. P. Levendorf, E. L. Spitler, V. B. Shields, M. G. Spencer, J. Park and W. R. Dichtel, *Science*, 2011, **332**, 228–231.
16 K. S. Novoselov, A. K. Geim, S. V. Morozov, D. Jiang, M. I. Katsnelson, I. V. Grigorieva, S. V. Dubonos and A. A. Firsov, *Nature*, 2005, **438**, 197–200.
17 J. M. Lu, O. Zheliuk, I. Leermakers, N. F. Q. Yuan, U. Zeitler, K. T. Law and J. T. Ye, *Science*, 2015, **350**, 1353–1357.
18 Y. Zhang, Y.-W. Tan, H. L. Stormer and P. Kim, *Nature*, 2005, **438**, 201–204.
19 F. Zhu, W. Chen, Y. Xu, C. Gao, D. Guan, C. Liu, D. Qian, S. Zhang and J. Jia, *Nat. Mater.*, 2015, **14**, 1020–1025.
20 S. B. Basuvalingam, Y. Zhang, M. A. Bloodgood, R. H. Godiksen, A. G. Curto, J. P. Hofmann, M. A. Verheijen, W. M. M. Kessels and A. A. Bol, *Chem. Mater.*, 2019, **31**, 9354–9362.
21 X. Li, W. Cai, J. An, S. Kim, J. Nah, D. Yang, R. Piner, A. Velamakanni, I. Jung, E. Tutuc, S. K. Banerjee, L. Colombo and R. S. Ruoff, *Science*, 2009, **324**, 1312–1314.
22 Y.-H. Lee, X.-Q. Zhang, W. Zhang, M.-T. Chang, C.-T. Lin, K.-D. Chang, Y.-C. Yu, J. T.-W. Wang, C.-S. Chang, L.-J. Li and T.-W. Lin, *Adv. Mater.*, 2012, **24**, 2320–2325.
23 K. Kang, S. Xie, L. Huang, Y. Han, P. Y. Huang, K. F. Mak, C.-J. Kim, D. Muller and J. Park, *Nature*, 2015, **520**, 656–660.
24 T. Ma, W. Ren, X. Zhang, Z. Liu, Y. Gao, L. C. Yin, X. L. Ma, F. Ding and H. M. Cheng, *Proc. Natl. Acad. Sci. U. S. A.*, 2013, **110**, 20386–20391.
25 W. Chen, J. Zhao, J. Zhang, L. Gu, Z. Yang, X. Li, H. Yu, X. Zhu, R. Yang, D. Shi, X. Lin, J. Guo, X. Bai and G. Zhang, *J. Am. Chem. Soc.*, 2015, **137**, 15632–15635.
26 Q. Ji, C. Su, N. Mao, X. Tian, J.-C. Idrobo, J. Miao, W. A. Tisdale, A. Zettl, J. Li and J. Kong, *Sci. Adv.*, 2021, **7**, eabj3274.
27 J. Xu and D. Ho, *Chem. Mater.*, 2021, **33**, 3249–3257.
28 P. Leidinger, J. Kraus and S. Gunther, *ACS Nano*, 2021, **15**, 12201–12212.
29 E. Pollmann, A. Maas, D. Marnold, A. Hucht, R.-M. Neubieser, M. Stief, L. Madauß and M. Schleberger, *2D Mater.*, 2022, **9**, 035001.
30 R. Ramachandramoorthy, R. Bernal and H. D. Espinosa, *ACS Nano*, 2015, **9**, 4675–4685.
31 Y. Zhu, D. Yuan, H. Zhang, T. Xu and L. Sun, *Nano Res.*, 2020, **14**, 1650–1658.
32 M. Zhang, E. A. Olson, R. D. Twesten, J. G. Wen, L. H. Allen, I. M. Robertson and I. Petrov, *J. Mater. Res.*, 2005, **20**, 1802–1807.
33 R. G. Spruit, J. T. van Omme, M. K. Ghatkesar and H. H. P. Garza, *J. Microelectromech. Syst.*, 2017, **26**, 1165–1182.
34 J. Zhao, L. Liang, S. Tang, G. Zhang, Y. Su, Y. Zhao, M. Li, L. Zhang, S. Fan, Q. Li and Y. Wei, *Nano Lett.*, 2023, **23**, 726–734.
35 X. Huang, R. Farra, R. Schlögl and M.-G. Willinger, *Nano Lett.*, 2019, **19**, 5380–5387.
36 W. Li, M. Li, X. Wang, P. Xu, H. Yu and X. Li, *Nano Today*, 2020, **35**, 100932.
37 D. M. Kirch, A. Ziemons, T. Burlet, I. Lischewski, X. Molodova, D. A. Molodov and G. Gottstein, *Rev. Sci. Instrum.*, 2008, **79**, 043902.
38 M. Munz, M. T. Langridge, K. K. Devarepally, D. C. Cox, P. Patel, N. A. Martin, G. Vargha, V. Stolojan, S. White and R. J. Curry, *ACS Appl. Mater. Interfaces*, 2013, **5**, 1197–1205.
39 R. Podor, N. Clavier, J. Ravaux, L. Claparede and N. Dacheux, *J. Am. Ceram. Soc.*, 2012, **95**, 3683–3690.
40 R. Podor, G. I. N. Bouala, J. Ravaux, J. Lautru and N. Clavier, *Mater. Charact.*, 2019, **151**, 15–26.
41 L. Joly-Pottuz, A. Bogner, A. Lasalle, A. Malchere, G. Thollet and S. Deville, *J. Microsc.*, 2011, **244**, 93–100.
42 G. Gregori, H. J. Kleebe, F. Siegelin and G. Ziegler, *J. Electron Microsc.*, 2002, **51**, 347–352.
43 K. Takahashi, K. Yamada, H. Kato, H. Hibino and Y. Homma, *Surf. Sci.*, 2012, **606**, 728–732.
44 P. R. Kidambi, B. C. Bayer, R. Blume, Z. J. Wang, C. Baehtz, R. S. Weatherup, M. G. Willinger, R. Schloegl and S. Hofmann, *Nano Lett.*, 2013, **13**, 4769–4778.
45 L. Wang, R. Lai, L. Zhang, M. Zeng and L. Fu, *ACS Mater. Lett.*, 2022, **4**, 528–540.
46 R. S. Weatherup, A. J. Shahani, Z. J. Wang, K. Mingard, A. J. Pollard, M. G. Willinger, R. Schloegl, P. W. Voorhees and S. Hofmann, *Nano Lett.*, 2016, **16**, 6196–6206.

47 Z. J. Wang, F. Ding, G. Eres, M. Antonietti, R. Schloegl and M. G. Willinger, *Adv. Mater. Interfaces*, 2018, **5**, 1800255.
48 M. S. Hoogeman, D. Glastra van Loon, R. W. M. Loos, H. G. Ficke, E. de Haas, J. J. van der Linden, H. Zeijlemaker, L. Kuipers, M. F. Chang and M. A. J. Klik, *Rev. Sci. Instrum.*, 1998, **69**, 2072.
49 M. J. Rosta, L. Crama, P. Schakel, E. van Tol, G. B. E. M. van Velzen-Williams, C. F. Overgauw, H. ter Horst, H. Dekker, B. Okhuijsen, M. Seynen, A. Vijftigschild, P. Han, A. J. Katan, K. Schoots, R. Schumm, W. van Loo, T. H. Oosterkamp and J. W. M. Frenken, *Rev. Sci. Instrum.*, 2005, **76**, 053710.
50 F. Esch, C. Dri, A. Spessot, C. Africh, G. Cautero, D. Giuressi, R. Sergo, R. Tommasini and G. Comelli, *Rev. Sci. Instrum.*, 2011, **82**, 053702.
51 L. L. Patera, F. Bianchini, G. Troiano, C. Dri, C. Cepek, M. Peressi, C. Africh and G. Comelli, *Nano Lett.*, 2015, **15**, 56–62.
52 G. Dong and J. W. M. Frenken, *ACS Nano*, 2013, **7**, 7028–7033.
53 L. L. Patera, C. Africh, R. S. Weatherup, R. Blume, S. Bhardwaj, C. Castellarin-Cudia, A. Knop-Gericke, R. Schloegl, G. Comelli, S. Hofmann and C. Cepek, *ACS Nano*, 2013, **7**, 7901–7912.
54 L. L. Patera, F. Bianchini, C. Africh, C. Dri, G. Soldano, M. M. Mariscal, M. Peressi and G. Comelli, *Science*, 2018, **359**, 1243–1246.
55 P. Arias, J. Tesař, A. Kavner, T. Šikola and S. Kodambaka, *ACS Nano*, 2019, **14**, 1141–1147.
56 P. Arias, A. Ebnonnasir, C. V. Ciobanu and S. Kodambaka, *Nano Lett.*, 2020, **20**, 2886–2891.
57 B. Chen, H. Zhang, J. Xuan, G. J. Offer and H. Wang, *Adv. Mater. Technol.*, 2020, **5**, 2000555.
58 A. A. Puretzky, D. B. Geohegan, S. Pannala, C. M. Rouleau, M. Regmi, N. Thonnard and G. Eres, *Nanoscale*, 2013, **5**, 6507–6517.
59 T. O. Terasawa and K. Saiki, *Nat. Commun.*, 2015, **6**, 6834.
60 H. R. Rasouli, N. Mehmood, O. Cakiroglu and T. S. Kasirga, *Nanoscale*, 2019, **11**, 7317–7323.
61 H. Xue, G. Wu, B. Zhao, D. Wang, X. Wu and Z. Hu, *ACS Appl. Electron. Mater.*, 2020, **2**, 1925–1933.
62 M. Jankowski, M. Saedi, F. La Porta, A. C. Manikas, C. Tsakonas, J. S. Cingolani, M. Andersen, M. de Voogd, G. J. C. van Baarle, K. Reuter, C. Galiotis, G. Renaud, O. V. Konovalov and I. M. N. Groot, *ACS Nano*, 2021, **15**, 9638–9648.
63 C. Lee, H. Yan, L. E. Brus, T. F. Heinz, J. Hone and S. Ryu, *ACS Nano*, 2010, **4**, 2695–2700.
64 K. P. Dhakal, G. Ghimire, K. Chung, D. L. Duong, S. W. Kim and J. Kim, *ACS Nano*, 2019, **13**, 14437–14446.
65 L. Sygellou, *Appl. Surf. Sci.*, 2019, **476**, 1079–1085.
66 M. Saedi, J. M. de Voogd, A. Sjardin, A. Manikas, C. Galiotis, M. Jankowski, G. Renaud, F. La Porta, O. Konovalov, G. J. C. van Baarle and I. M. N. Groot, *Rev. Sci. Instrum.*, 2020, **91**, 013907.
67 P. Leidinger, M. Panighel, V. Pérez Dieste, I. J. Villar-Garcia, P. Vezzoni, F. Haag, J. V. Barth, F. Allegretti, S. Günther and L. L. Patera, *Nanoscale*, 2023, **15**, 1068–1075.
68 O. V. Konovalov, V. Belova, F. La Porta, M. Saedi, I. M. N. Groot, G. Renaud, I. Snigireva, A. Snigirev, M. Voevodina, C. Shen, A. Sartori, B. M. Murphy and M. Jankowski, *J. Synchrotron Radiat.*, 2022, **29**, 711–720.
69 M. Losurdo, M. Giangregorio, M. P. Capezzuto and G. Bruno, *J. Phys. Chem. C*, 2011, **115**, 21804–21812.
70 Y. Wang, L. Zhang, C. Su, H. Xiao, S. Lv, F. Zhang, Q. Sui, L. Jia and M. Jiang, *Nanomaterials*, 2019, **9**, 1640.
71 C. Gong, K. He, G. D. Lee, Q. Chen, A. W. Robertson, E. Yoon, S. Hong and J. H. Warner, *ACS Nano*, 2016, **10**, 9397–9410.
72 J. Huang, Z. Zhang, Y. Ying, M. Gan, H. Huang and L. Fei, *Chem. Commun.*, 2022, **58**, 9746–9749.
73 Z.-J. Wang, G. Weinberg, Q. Zhang, T. Lunkenbein, A. Klein-Hoffmann, M. Kurnatowska, M. Plodinec, Q. Li, L. Chi, R. Schloegl and M.-G. Willinger, *ACS Nano*, 2015, **9**, 1506–1519.
74 Z. Liu, Y. C. Lin, C. C. Lu, C. H. Yeh, P. W. Chiu, S. Iijima and K. Suenaga, *Nat. Commun.*, 2014, **5**, 4055.
75 L. Wang, Y. Ding, X. Wang, R. Lai, M. Zeng and L. Fu, *Adv. Sci.*, 2021, **8**, 2100334.
76 K. Zhang, C. Ding, B. Pan, Z. Wu, A. Marga, L. Zhang, H. Zeng and S. Huang, *Adv. Mater.*, 2021, **33**, 2105079.
77 C. Tsakonas, A. C. Manikas, M. Andersen, M. Dimitropoulos, K. Reuter and C. Galiotis, *Chem. Eng. J.*, 2021, **421**, 129434.
78 S. Hussain, R. Zhou, Y. Li, Z. Qian, Z. Urooj, M. Younas, Z. Zhao, Q. Zhang, W. Dong, Y. Wu, X. Zhu, K. Wang, Y. Chen, L. Liu and L. Xie, *J. Am. Chem. Soc.*, 2023, **145**, 11348–11355.
79 L. Xie, Z. Zhi and Z. Zhao, *China Pat*, 202110662304, 2022.
80 G. Dong, E. B. Fourre, F. C. Tabak and J. W. Frenken, *Phys. Rev. Lett.*, 2010, **104**, 096102.
81 Z.-J. Wang, J. Dong, L. Li, G. Dong, Y. Cui, Y. Yang, W. Wei, R. Blume, Q. Li, L. Wang, X. Xu, K. Liu, C. Barroo, J. W. M. Frenken, Q. Fu, X. Bao, R. Schlogl, F. Ding and M.-G. Willinger, *ACS Nano*, 2020, **14**, 1902–1918.
82 D. Geng, B. Wu, Y. Guo, L. Huang, Y. Xue, J. Chen, G. Yu, L. Jiang, W. Hu and Y. Liu, *Proc. Natl. Acad. Sci. U. S. A.*, 2012, **109**, 7992–7996.
83 S. Y. Cho, M. S. Kim, M. Kim, K. J. Kim, H. M. Kim, D. J. Lee, S. H. Lee and K. B. Kim, *Nanoscale*, 2015, **7**, 12820–12827.
84 J. S. Lee, S. H. Choi, S. J. Yun, Y. I. Kim, S. Boandoh, J.-H. Park, B. G. Shin, H. Ko, S. H. Lee, Y.-M. Kim, Y. H. Lee, K. K. Kim and S. M. Kim, *Science*, 2018, **362**, 817–821.
85 Y. He, P. Tang, Z. Hu, Q. He, C. Zhu, L. Wang, Q. Zeng, P. Golani, G. Gao, W. Fu, Z. Huang, C. Gao, J. Xia, X. Wang, X. Wang, C. Zhu, Q. M. Ramasse, A. Zhang, B. An, Y. Zhang, S. Marti-Sanchez, J. R. Morante, L. Wang, B. K. Tay, B. I. Yakobson, A. Trampert, H. Zhang, M. Wu,

Q. J. Wang, J. Arbiol and Z. Liu, *Nat. Commun.*, 2020, **11**, 57.
86 W. Yao, B. Wu and Y. Liu, *ACS Nano*, 2020, **14**, 9320–9346.
87 S. Kodambaka, D. L. Chopp, I. Petrov and J. E. Greene, *Surf. Sci.*, 2003, **540**, L611–L616.
88 X. Sang, X. Li, A. A. Puretzky, D. B. Geohegan, K. Xiao and R. R. Unocic, *Adv. Funct. Mater.*, 2019, **29**, 1902149.
89 Y. Liu, L. Xu, L. Zhang, Z. Dong, S. Wang and L. Luo, *ACS Appl. Mater. Interfaces*, 2020, **12**, 52201–52207.
90 P. W. Sutter, J. I. Flege and E. A. Sutter, *Nat. Mater.*, 2008, **7**, 406–411.
91 S. Günther, S. Danhardt, B. Wang, M. L. Bocquet, S. Schmitt and J. Wintterlin, *Nano Lett.*, 2011, **11**, 1895–1900.
92 X. Yang, Y. Liu, H. Q. Ta, E. Rezvani, Y. Zhang, M. Zeng, L. Fu, A. Bachmatiuk, J. Luo, L. Liu and M. H. Rümmeli, *npj 2D Mater. Appl.*, 2021, **5**, 91.
93 W. L. Wang, E. J. Santos, B. Jiang, E. D. Cubuk, C. Ophus, A. Centeno, A. Pesquera, A. Zurutuza, J. Ciston, R. Westervelt and E. Kaxiras, *Nano Lett.*, 2014, **14**, 450–455.
94 J. Zhao, Q. Deng, S. M. Avdoshenko, L. Fu, J. Eckert and M. H. Rummeli, *Proc. Natl. Acad. Sci. U. S. A.*, 2014, **111**, 15641–15646.
95 H. Q. Ta, L. Zhao, W. Yin, D. Pohl, B. Rellinghaus, T. Gemming, B. Trzebicka, J. Palisaitis, G. Jing, P. O. Å. Persson, Z. Liu, A. Bachmatiuk and M. H. Rümmeli, *Nano Res.*, 2018, **11**, 2405–2411.
96 X. Yang, H. Q. Ta, H. Hu, S. Liu, Y. Liu, A. Bachmatiuk, J. Luo, L. Liu, J. H. Choi and M. H. Rummeli, *Adv. Funct. Mater.*, 2021, **31**, 2104340.
97 R. S. Weatherup, B. C. Bayer, R. Blume, C. Ducati, C. Baehtz, R. Schlogl and S. Hofmann, *Nano Lett.*, 2011, **11**, 4154–4160.
98 R. S. Weatherup, B. C. Bayer, R. Blume, C. Baehtz, P. R. Kidambi, M. Fouquet, C. T. Wirth, R. Schlögl and S. Hofmann, *ChemPhysChem*, 2012, **13**, 2544–2549.